

Diagnostic detection of diffuse glioma tumors *in vivo* with molecular fluorescent probe-based transmission spectroscopy

Summer L. Gibbs-Strauss^{a)}

Thayer School of Engineering, Dartmouth College, Hanover, New Hampshire 03755-8000

Julia A. O'Hara

*Thayer School of Engineering, Dartmouth College, Hanover, New Hampshire 03755-8000
and Department of Diagnostic Radiology, Dartmouth Medical School, Lebanon New Hampshire 03756*

Subhadra Srinivasan

Thayer School of Engineering, Dartmouth College, Hanover, New Hampshire 03755-8000

P. Jack Hoopes

*Thayer School of Engineering, Dartmouth College, Hanover, New Hampshire 03755-8000
and Department of Surgery, Dartmouth Medical School, Lebanon New Hampshire 03756*

Tayyaba Hasan

*Department of Dermatology, Harvard Medical School and Wellman Center for Photomedicine,
Massachusetts General Hospital, Boston, Massachusetts 02114*

Brian W. Pogue

*Thayer School of Engineering, Dartmouth College, Hanover, New Hampshire 03755-8000;
Department of Surgery, Dartmouth Medical School, Lebanon New Hampshire 03756;
and Wellman Center for Photomedicine, Massachusetts General Hospital, Boston, Massachusetts 02114*

(Received 19 August 2008; revised 30 November 2008; accepted for publication 23 December 2008; published 25 February 2009)

The diffuse spread of glioma tumors leads to the inability to image and properly treat this disease. The optical spectral signature of targeted fluorescent probes provides molecular signals from the diffuse morphologies of glioma tumors, which can be a more effective diagnostic probe than standard morphology-based magnetic resonance imaging (MRI) sequences. Three orthotopic xenograft glioma models were used to examine the potential for transmitted optical fluorescence signal detection *in vivo*, using endogenously produced protoporphyrin IX (PpIX) and exogenously administered fluorescently labeled epidermal growth factor (EGF). Accurate quantification of the fluorescent signals required spectral filtering and signal normalization, and when optimized, it was possible to improve detection of sparse diffuse glioma tumor morphologies. The signal of endogenously produced PpIX provided similar sensitivity and specificity to MRI, while detection with fluorescently labeled EGF provided maximal specificity for tumors with high EGF receptor activity. Optical transmitted fluorescent signal may add significant benefit for clinical cases of diffuse infiltrative growth pattern glioma tumors given sufficient optimization of the signal acquisition for each patient. © 2009 American Association of Physicists in Medicine. [DOI: 10.1118/1.3075770]

Key words: glioma, imaging, fluorescence, protein, magnetic resonance

I. INTRODUCTION

In this study, a spectrally resolved approach to detection of two different targeted fluorescent proteins was analyzed for the sensitivity and specificity of detecting glioma tumors with different structural morphologies. Clinically, glioma tumors are diagnosed with contrast MR or CT, yet it is well known that the sensitivity and specificity of these diagnostic procedures are not always near the ideal values,^{1,2} which is especially true for brain stem glioma with a diffuse pattern of growth.³ Measurements of fluorescence were analyzed in conjunction with magnetic resonance (MR) imaging of pertinent xenograft glioma models to examine the conditions where MR and optical signals provide complementary information, particularly for diffuse tumor morphologies which contribute to some of the most difficult cases to diagnose and treat.^{3,4} The molecular signature of the tumor was measured

optically using two molecularly targeted probes; one specific for cellular metabolism and the other for tracking epidermal growth factor receptor (EGFR) tumor status. Aminolevulinic acid was administered to tumor-bearing animals prior to measurement of endogenously produced protoporphyrin IX, which is well known to produce significant signal that has shown success in guiding glioma surgery, yet has not been examined for glioma diagnostic work.^{5,6} The second approach examined exogenously administered epidermal growth factor (EGF) labeled with a near-infrared fluorescent tag, and this approach was chosen due to the overexpression of EGFR in many glioma tumors. The transmitted fluorescence signal was spectrally resolved, and the signal intensities were normalized to the transmitted excitation light signals to make it more robust and less sensitive to positioning and tissue shape. These specific tumor models were chosen

to illustrate and examine which fluorescent proteins were most beneficial, and the two choices examined were related to known protein contrast mechanisms specific for glioma tumors.^{7,8} Most implanted murine brain tumor models grow as large bulk masses that significantly disturb the brain structure and are readily detectable by structural based imaging techniques such as standard MRI and CT. The rationale for this work was that optical signals are diffusely transmitted, and thus could provide contrast even when the tumor had a diffuse scattered morphology.

II. METHODS

II.A. Fluorescence modeling

A three dimensional (3D) mouse head model was constructed from 745 computed tomography (CT) slices, with 0.047 mm resolution, of a male nude mouse head collected using a eXplore Locus preclinical *in vivo* MicroCT Scanner (GE Healthcare, Ontario, Canada). This data set was used to create a 3D volumetric mesh through image segmentation, using the medical imaging software MIMICS™ (Materialise, Inc.) and geometry description. The outer surface of the mouse head as well as the interior regions of brain, bone, and skin were segmented using this software [Fig. 1(a)]. The outer head surface was exported in sterolithography format and meshed into a tetrahedral finite element mesh using meshing software NETGEN, with a maximum element size of 0.8 mm. The mesh contained 86 927 tetrahedral elements corresponding to 18 662 nodes and was tagged with different material properties for the areas of brain, bone, skin, and adipose tissue [Fig. 1(b)]. These regions of the mesh were suitably labeled with corresponding optical properties at the excitation and emission wavelengths from literature.^{9,10} This mesh was used for further computation, which is described as follows.

The NIRFAST light diffusion modeling package was used to simulate light fluence rate of the laser source and the emitted fluorescence wavelengths in tissue.¹¹ The two source-detector configurations used for *in vivo* experiments were modeled to compare the ability to detect tumors of varied sizes, contrasts, and positions. Results with two fiber optic source-detector configuration, simulating the single channel spectroscopy system [Fig. 1(c)], were compared to results obtained with eight fiber optic source-detector configuration, simulating the multichannel spectroscopy system [Fig. 1(d)]. In each case, the fiber optic could act as either a source or a detector, but not simultaneously. Thus, for the two fiber optic configuration two measurements were obtained from the model, while for the eight fiber optic configuration, 56 measurements were obtained from the model. For both fiber optic configurations the obtained measurements were averaged into a single number to be compared between animals. For control mice, an anomaly was not included in the mesh and the light fluence rate of the excitation and the emitted wavelength in the tissue was modeled. A spherical anomaly with a radius of 0.5–5 mm increased by 0.5 mm increments was used to simulate a growing tumor. Fluorescence contrast ratios of 2:1, 3:1, 4:1, 5:1, 7:1, and 10:1 tumor tissue to normal

tissue were modeled for each tumor size. In this study two tumor positions were modeled which included the tumor at the center of the brain and a more realistic case of the tumor of 1 mm in on all axes from the top, left edge of the brain. The area under the curve at the excitation wavelength and the emission wavelength were calculated so that data could be reported as a single number representing the fluorescence to transmittance ratio. To determine the difference in signal intensity between a tumor-bearing mouse and a non-tumor-bearing mouse, the fluorescence to transmittance ratio of a control mouse was subtracted from an anomaly-bearing mouse. This quantity was then normalized by the signal intensity of the control mouse.

II.B. Cell culture

Three cell lines were used in the current study; the 9L-GFP rat gliosarcoma line which had been transfected with green fluorescent protein (GFP),¹² the U251 human glioma line and the GFP variant of this cell line which was transfected in the laboratory (U251-GFP). The U251 parent line was transfected using the pAcGFP1-N1 vector (Clontech), Lipofectin Reagent (Invitrogen, Carlsbad, CA), and Geneticin selective antibiotic (Invitrogen, Carlsbad, CA) at a concentration of 700 $\mu\text{g}/\text{ml}$ in the growth medium. The cells were transfected according to the manufacture instructions and grown in selection media during three rounds of selection via a FACS Aria (Becton Dickinson, San Jose, CA). All stable cell lines were grown in Dulbecco's modification of eagle's medium (DMEM) supplemented with 10% fetal bovine serum (FBS) and 1% penicillin/streptomycin from a stock solution of 10 000 IU penicillin and 10 000 $\mu\text{g}/\text{ml}$ streptomycin (Mediatech, Inc., Herndon, VA). Cells were incubated at 37 °C in a 95% air and 5% carbon dioxide humidified environment.

II.C. Murine glioma model

The three cell lines described previously (9L-GFP, U251, U251-GFP) were used for intracranial implantation. Cells were implanted at 1×10^6 in 10 μl of phosphate buffered saline (PBS) via a Hamilton syringe. Male athymic nude mice about 6 weeks in age were used in all studies. The mice were anesthetized with a ketamine/xylazine mixture administered intraperitoneally (IP) in a 90:10 mg/kg ratio. Their body temperature was maintained using a heating pad during the surgical procedure. A small incision was made through the scalp, exposing the skull. A dremel drill with a 1 mm diameter bit was used to create a hole 2 mm behind the bregma and 2 mm to the left of the midline. The Hamilton syringe was inserted stereotactically through the hole, 2 mm deep into the brain tissue where the cells were deposited over a 5 min period. Following the injection, the needle was slowly removed and the skull and scalp were cleaned. Bone wax was used to close the hole in the skull and Vetbond (J.A. Webster, Inc., Sterling, MA) was used to close the incision in the scalp. Mice were examined daily to ensure proper healing

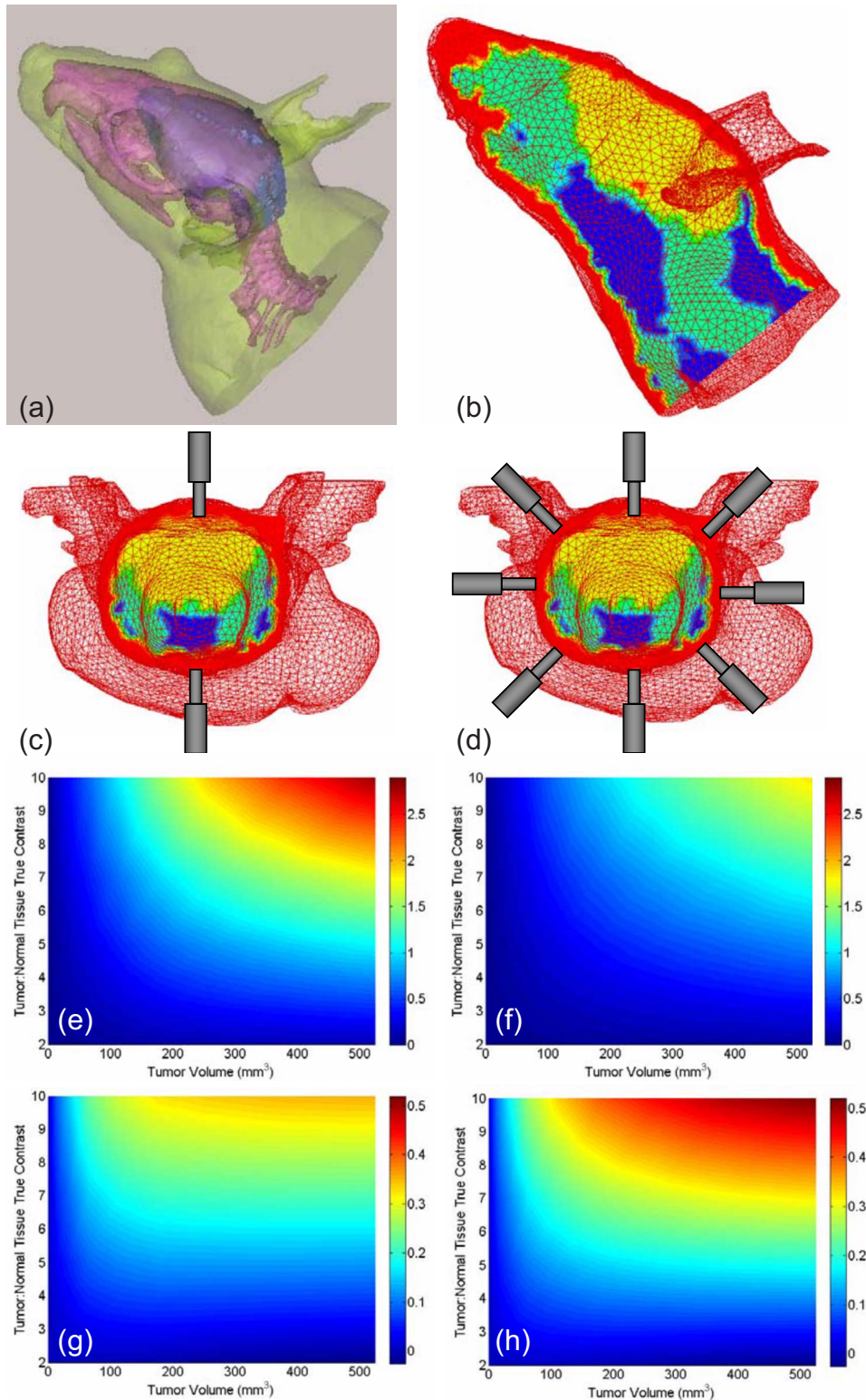


FIG. 1. (a) Segmented mouse head boundary with skin, brain, and bone regions defined. (b) Mouse head mesh with slice showing the skin, brain, bone, and adipose regions. In (c) a fiber optic source-detector pair is shown for transmittance measurement. In (d) positioning of eight fiber optics are shown. The signal relative to tumor size and the tumor contrast is plotted with the measured contrast in the color scales of (e)–(h). In (e) is the contrast with tumor positioned at the center of brain using a single source-detector pair for measurement. In (f) the same tumor position was used, with eight sources and detectors and averaged measurements. In (g) the contrast from an off center tumor, using a single source-detector pair is shown, and in (h) the signal from the off center tumor is shown with all eight fiber measurements averaged together.

of the scalp. All control mice were implanted with 10 μ l of PBS without cells to mimic the surgical procedures performed on the tumor-bearing mice.

II.D. Fluorescence spectroscopy systems

Two transmission fluorescence spectroscopy systems were used in these studies: a single channel system and a multi-

channel system. The protoporphyrin IX fluorescence data were collected using the single channel spectroscopy system consisting of a single spectrometer (1200 l/mm grating, SpectraPro 300, Acton Research, Acton MA) coupled to a CCD camera (Spec-10:400BR/XTE, Princeton Instruments, Acton MA) cooled to -90 °C, a 2 W 635 nm diode laser system (Power Technology, Alexander AR), and a light tight

box for mouse measurements. The light from the 635 nm laser was collimated onto the chin of the mouse and a second collimator was placed opposite the laser light on the head of the mouse, where the light was passed through a 650 nm LP filter and into the spectrometer. The light was detected after passing through the spectrometer and onto a cooled CCD camera, where it was captured and transferred using commercially supplied software (WINSPEC, Acton Research). The spectrometer was centered at 705 nm to collect PpIX fluorescence emission data and at 615 nm to collect the transmitted excitation light from the laser. At each time point the mouse was placed in the light tight box where fluorescence and transmittance measurements were collected prior to any movement of the mouse. The EGF fluorescence data were acquired using the multichannel transmission spectroscopy system which has been described in detail previously.¹³ Briefly this system consisted of eight spectrometers used in the current study and a continuous wavelength of 690 nm laser coupled into a rotary stage. Each spectrometer had a filter wheel containing a 720 nm LP filter and a 2 OD filter used in this study. The system was controlled through LABVIEW based software.

The spectrometers were centered at 820 nm to collect epidermal growth factor (EGF) conjugated IRDye 800CW (EGF-IRDye) (LI-COR Biosciences, Lincoln, NE) emission data and at 690 nm to collect the transmission data. The emission data set was collected using the 720 nm LP filter and the 300 1/mm grating while the transmission data set was collected using the 2 OD filter and the 1200 1/mm grating. A mouse holder was constructed from liquid epoxy/resin¹⁴ using a silicon mouse prototype to obtain a "mouse-shaped" mold allowing for repeatable fiber placement around the head.

The raw excitation and emission data obtained from spectroscopy were postprocessed through spectral fitting followed by normalization. The raw fluorescence emission data were spectrally fitted using a MATLAB program to do a linear least-squares fitting to appropriate phantom data to deconvolve the fluorescence signal from any bleed through signal. Both the spectrally fitted emission data and the excitation data were normalized to counts per second accounting for varied exposure times. The excitation spectrum was used to integrate the area under the laser peak. Then, the spectrally fitted fluorescence data were normalized to the integrated excitation data yielding the fluorescence to transmittance ratio. Following normalization the fluorescence spectra were integrated providing one number representing the area under the curve, which could be compared between animals.

II.E. MRI of murine brain tumors

MR imaging was completed using a Philips 3T Achieva MRI scanner, with a research rodent coil insert designed specifically for imaging mice and rats. T1 turbospin echo (TSE) contrast enhanced (CE) with gadolinium DTPA and T2 TSE sequences were routinely used to visualize brain structure and vascular volume changes due to tumor growth. T1 TSE images were collected before and after gadolinium adminis-

tration via an IP catheter, enabling T1 difference images to be calculated and used to increase the ability to visualize gadolinium uptake. Additional sequences were adapted for mouse imaging from standard sequences. The most successful of these sequences included T2 fluid attenuated inversion recovery (FLAIR), T1 inversion recovery (IR), and T1 fast field echo (FFE). Parameters such as slice thickness, field of view, and the size of the reconstruction matrix were varied and tested to allow acquisition of the qualitatively best image. Analysis of MRI visibility of the three brain tumor models was completed by measuring the intensity in a region of interest in the tumor and a similar region of interest in the normal, contralateral side of the brain. The tumor tissue to normal tissue contrast was calculated using this analysis for at least five MRI slices per imaging sequence per animal. For control animals, the signal intensity in a similar region of interest in each hemisphere of the brain was used to calculate a comparable contrast ratio.

II.F. Fluorescence detection of murine brain tumors

Two fluorophores were used for fluorescence detection of murine brain tumors including an intracellular and extracellular fluorophores. The prodrug aminolevulinic acid (ALA), which is converted intracellularly to fluorescently detectable protoporphyrin IX (PpIX) via the heme synthesis pathway, was monitored using the single channel spectroscopy system. Prior to ALA administration mice were placed in the fluorescence spectroscopy system to measure their endogenous background PpIX fluorescence. Following background PpIX measurements, 100 mg/kg ALA was administered IP to all mice prior to exogenous PpIX fluorescence measurements. Two hours after ALA administration the mice were placed back in the spectroscopy system where their fluorescence and transmittance were again measured. Finally, the brain was extracted and placed into the spectroscopy system for *ex vivo* PpIX measurements of the brain tumors *in situ*. The brains were then sectioned coronally and imaged for PpIX fluorescence in each slice on a reflectance raster scanner (Typhoon 9410 variable mode imager, GE Life Sciences) using a 635 nm laser for excitation and 650 nm LP filter for emission. The GFP transfected tumors were also imaged for GFP fluorescence on the reflectance raster scanner using a 488 nm laser for excitation and a 526 nm short pass filter for emission prior to movement of the tissue sample. All *ex vivo* samples were preserved in 10% formalin and stained with hematoxylin and eosin (HE).

The multichannel spectroscopy system was used to monitor EGF-IRDye fluorescence 24 after IV administration of 1 nmole EGF-IRDye.¹⁵ The multichannel transmission spectroscopy system enabled collection of 56 measurement points from around the head for all animals. The average of the control mice ($n=8$) was calculated at each of the 56 points. All mice were normalized to the average of the control animals by subtracting the average control mouse data and dividing the result by the average control mouse data on a point-by-point basis. The 56 normalized data points were then averaged into a single number providing a robust fluo-

rescence signal from around the mouse head. Following *in vivo* measurements the mice were sacrificed, their brains extracted and sectioned coronally into quarters. The brain sections were imaged for EGF-IRDye fluorescence on the Odyssey Infrared Imaging System (LI-COR Biosciences, Lincoln, NE) using the 800 nm channel and for GFP fluorescence on the reflectance raster scanner, after which the brains were preserved in 10% formalin for HE staining.

III. RESULTS

III.A. Optical detection simulation study

One important issue about how light measurements would be optimally used to detect tumor tissues is the logistical problem of how to bring light in and out of the tissue routinely, in a robust and maximally sensitive manner. Light transport modeling studies were used to analyze this strategy looking at the murine geometry for tumors in the brain of different sizes and contrasts (Fig. 1).^{13,16} The excitation light signal input was transmitted through the head in a diffuse manner, and the fluorescence signal was also highly diffused as it was generated. Quantitative detection of a tumor inside the cranium was analyzed by plotting the calculated fluorescence to transmittance ratio signal, normalized by the signal without a tumor. The two tumor positions examined were (i) at the center of the brain and (ii) 1 mm in from the top, left edge of the brain on all axes. The average of all collected measurements including different fiber geometries are reported in Figs. 1(e)–1(h). When the tumor was positioned in the fiber plane, tumor detection was better using the two fiber optic configuration [Fig. 1(e)] than the eight fiber optic configuration [Fig. 1(f)]. Therefore, the transmission measurement directly across the mouse head showed the largest difference in signal intensity when compared to the control mouse. Averaging the light path with the largest contrast with additional measurements that sampled varied parts of the brain tissue confounded the signal in comparison to measurements directly across the tumor. However, in the more realistic case where the tumor was not directly in the plane of the fiber optics, detection was better using the eight fiber optic configuration [Fig. 1(h)] than the two fiber optics [Fig. 1(g)], since this geometry sampled varied light paths across the brain. This simulation illustrated the extreme positional sensitivity of optical transmission measurements when the tumor position is not exactly known.

III.B. Analysis of glioma model morphology and MR detection

MR detection of the three tumor types (9L-GFP, U251 and U251-GFP) was cell line dependent due to significant differences in growth pattern in the brain. The 9L-GFP and U251 tumors grew in solid masses, which appeared to have substantial breakdown of the blood brain barrier, while the U251-GFP tumors had a much different growth pattern. Three example mice with the U251-GFP tumor can be seen in Fig. 2, where the bottom two rows illustrate T1 turbo spin echo (TSE) contrast enhanced (CE) MRI. The MR images in

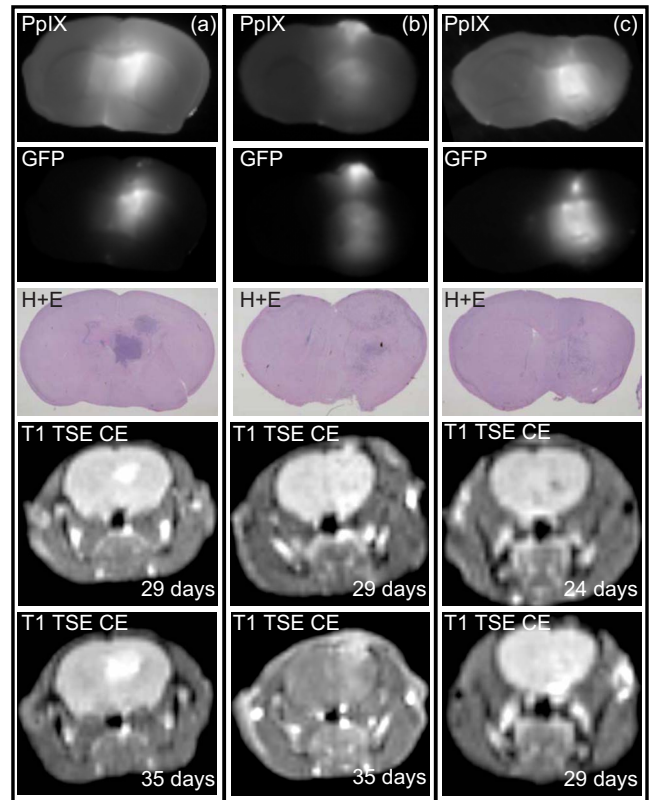


Fig. 2. Three representative examples of mice implanted with U251-GFP brain tumors. The first three rows illustrate *ex vivo* data, with the top row showing PpIX fluorescence and the second row showing GFP fluorescence and the third row showing the corresponding H+E image. The bottom two rows illustrate *in vivo* T1 turbo spin echo (TSE) contrast enhanced (CE) MRI, with the next to the bottom row showing MRI 29 days after tumor implantation and the bottom row showing MRI 35 days following implantation. All three cases show that the PpIX fluorescence images, the GFP images and H+E images show tumor at the same location. The MRI image in (a) shows the tumor is well demarcated by T1 TSE CE MRI. However, this is an anomalous case and most U251-GFP tumors are most similar to those shown in (b) and (c) where the tumor is not well demarcated in the T1 TSE CE MRI and very difficult to visualize.

Fig. 2(a) enabled detection of the U251-GFP tumor at 29 and 35 days following implantation. However, this was anomalous for the U251-GFP tumor type and in most U251-GFP implanted mice the T1 TSE CE MR images did not enable reliable detection of the tumor tissue from the normal brain tissue [Figs. 2(b) and 2(c)]. In most cases, even if a suspected region was present in the MR, the tumor boundaries were blurry such that shapes and volumes could not be visualized accurately. MR imaging readily detected both the U251 and 9L-GFP implanted tumors. Representative sample 9L-GFP tumors, shown in Fig. 3 (bottom row), had significant contrast compared to the normal brain tissue by T1 TSE CE MRI 21 days following implantation. In contrast to the U251-GFP tumor-bearing mice, all three example 9L-GFP tumor-bearing mice had tumor tissue that was well demarcated by T1 TSE CE MRI, such that size and volume could be easily visualized.

The contrast of each tumor type by MRI was calculated using the tumor to normal tissue ratio for each image sequence. The tumor to normal tissue contrast ratio for the

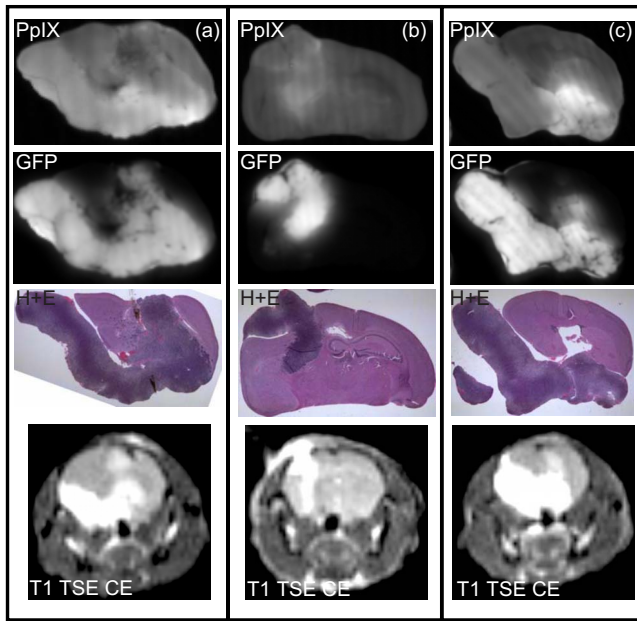


FIG. 3. Three representative examples of mice implanted with 9L-GFP brain tumors. The first three rows illustrate *ex vivo* data, with the top row showing PpIX fluorescence, the second row showing GFP fluorescence, and the third row showing the corresponding H+E image. The bottom row illustrate *in vivo* T1 turbospin echo (TSE) contrast enhanced (CE) MRI. In (a) it can be seen that the PpIX fluorescence is largely confined to the bulk tumor, although a portion of the tumor tissue does not appear to have PpIX production as compared to the corresponding GFP and H+E images. However, most of the examples of this tumor line show PpIX production patterns more similar to those illustrated in (b) and (c) where the PpIX fluorescence is only in the periphery of the tumor tissue and not necessarily in the bulk tumor. As can be seen in (a)–(c), the 9L-GFP tumor is well demarcated by T1 TSE CE MRI.

9L-GFP, U251, U251-GFP, and non-tumor-bearing control animals are shown in Figs. 4(a) and 4(b) for the T1 TSE CE and T2 TSE MRI, respectively. The U251-GFP tumor to normal tissue contrast was further assessed for T1 difference, T2 FLAIR, T1 IR, and T1 FFE MRI to determine if these alternate MRI sequences increased the tumor to normal tissue contrast compared to standard sequences [Fig. 4(c)]. The 9L-GFP and U251 brain tumors had higher tumor to normal tissue contrast with T1 TSE CE MRI than the control mice (mean tumor to normal tissue contrast: 9L-GFP=1.41, U251=1.30, control=0.98 [Fig. 4(a)]). In comparison, the tumor to normal tissue contrast of the U251-GFP brain tumors by T1 TSE CE-MRI was very similar to that of the control mice (mean tumor to normal tissue contrast: U251-GFP=1.04 [Fig. 4(a)]. Both the 9L-GFP and U251 brain tumors also had greater contrast as compared to control mice by T2 TSE MRI, while the U251-GFP brain tumors again showed very similar contrast to the control mice (mean tumor to normal tissue contrast: 9L-GFP=1.26, U251=1.46, U251-GFP=1.00, control=0.97 [Fig. 4(b)].

The difference in MRI detection was more comprehensively assessed through receiver operator characteristic (ROC) curves, which were constructed from the contrast data using a parametric model-based ROC analysis¹⁷ where each analysis was summarized by the area under the curve (AUC).

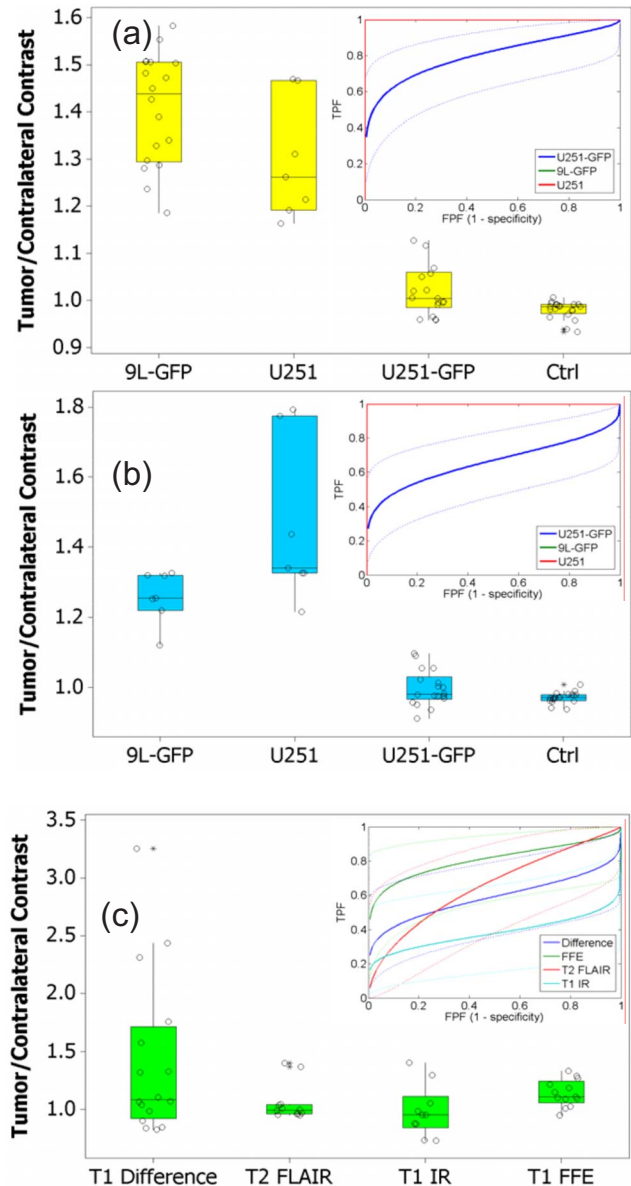


FIG. 4. All graphs show tumor signal/signal on contralateral side of brain, with an inset ROC curve comparing the control animals with each tumor-bearing group. (a) T1 TSE CE MRI for 9L-GFP, U251, and U251-GFP tumor-bearing mice. The control mice did not have implanted tumors, but did have sham surgery. (b) T2 TSE MR for 9L-GFP, U251, U251-GFP, and control mice. The T1 TSE CE and T2 TSE MRI allow for visualization of the 9L-GFP and U251 tumor-bearing mice as compared to the control mice. However, both conventional imaging sequences fail to discern the U251-GFP tumors in the mice. Additional MR imaging sequences were conducted for the U251-GFP mice, the contrasts of which are illustrated in (c). The MRI sequences included T1 TSE with contrast and T1 TSE without contrast, providing the ability for difference imaging, T1 fast field echo (FFE), T2 fluid attenuated inversion recovery (T2 FLAIR), and T1 inversion recovery (T1 IR).

The true positive fraction (TPF) and the false positive fraction (FPF) values were plotted for both T1 TSE CE and T2 TSE MRI. T1 TSE CE and T2 TSE MRI had perfect ROC curves for the 9L-GFP and U251 where the AUC was equal to one indicating that tumors could be detected with 100% sensitivity and specificity at all thresholds [Figs. 4(a) and 4(b)]. Conversely, the U251-GFP tumors were difficult to

detect by both T1 TSE CE and T2 TSE MRI, as illustrated by the ROC curves in Fig. 4. T1 TSE CE-MRI provided slightly better detection (AUC=0.80) than T2 TSE MRI (AUC=0.67) of the U251-GFP tumors.

Due to the inability to reliably detect the U251-GFP brain tumors by conventional T1 TSE CE and T2 TSE MRI, additional MRI sequences were used to try to gain contrast in the tumor tissue over the normal tissue. T1 TSE sequences were collected prior to the administration of the contrast agent and again after the administration of the contrast agent without movement of the mouse to allow for difference imaging. As can be seen in Fig. 4(c), difference imaging showed increased contrast in some of the U251-GFP brain tumors over that of the control mice, but did not allow for visualization of all tumors of this variety. T1 fast field echo (FFE), T2 fluid attenuated inversion recovery (T2 FLAIR), and T1 inversion recovery (T1 IR) were also tried, with marginal success on average [Fig. 4(c)]. ROC curves were also constructed for these sequences and compared via area under the curve. U251-GFP tumor detection via T1 FFE (AUC=0.81) was similar to that of T1 TSE CE MRI. U251-GFP tumor detection via T1 difference (AUC=0.59), T2 FLAIR (AUC=0.65), and T1 IR (AUC=0.38) were worse than detection via T2 TSE and thus largely unsuccessful.

III.C. Analysis of endogenously produced PpIX fluorescence detection of glioma models

The three tumor types (9L-GFP, U251, U251-GFP) were measured optically with the single channel spectroscopy system, using endogenously produced PpIX following ALA administration, which is known to be abundant in glioma tumors relative to normal brain. The PpIX fluorescence of each mouse was normalized to the average PpIX fluorescence of the control mice ($n=18$) and the mean PpIX fluorescence of each tumor type was significantly higher than the control mean PpIX fluorescence 2 h after the administration of 100 mg/kg ALA (p -value between control group: 9L-GFP=0.037, U251=0.010, U251-GFP=0.027). The normalized mean PpIX fluorescence 2 h after that administration of ALA was 1.0 for the control group, 1.28 for the 9L-GFP, 1.49 for the U251, and 1.17 for the U251-GFP tumor-bearing groups [Fig. 5(a)]. By ROC analysis, *in vivo* PpIX spectroscopy was better able to detect the U251 (AUC=0.78) and U251-GFP (AUC=0.79) than the 9L-GFP (AUC=0.59) tumor-bearing mice [Fig. 5(a)]. After spectroscopy measurements were completed the brains were sectioned coronally and imaged using a raster scanning system. Three representative examples of the PpIX fluorescence in a coronal section of a representative U251-GFP sample tumor can be seen in the top row of Fig. 2. The PpIX fluorescence was contained within the bulk tumor region of the three mice shown as can be seen when the images were compared with corresponding GFP and HE images (Fig. 2, second and third row). In contrast, when the 9L-GFP tumor-bearing mice were considered, the PpIX fluorescence was sometimes contained within the bulk tumor tissue [Fig. 3(a)], but more often was only seen at the periphery of the tumor tissue [Figs. 3(b) and 3(c)].

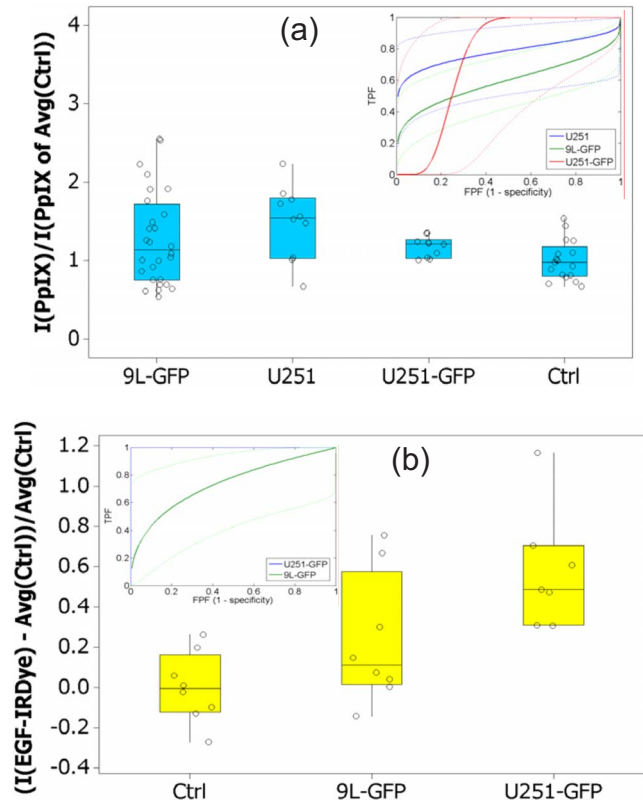


Fig. 5. PpIX and EGF-IRDye fluorescence spectroscopy measurements were collected for mice with diffuse growing and bulk growing tumor tissue. (a) *In vivo* PpIX fluorescence 2 h after the administration of ALA. (b) *In vivo* EGF-IRDye fluorescence 24 h following intravenous administration. ROC curves are inset to illustrate detection of each tumor type over non-tumor-bearing control mice for each fluorophore.

III.D. Analysis of targeted growth factor fluorescence detection of glioma models

The multichannel spectroscopy system was used to assess fluorescence signature differences between the 9L-GFP and U251-GFP intracranial tumors using fluorescently labeled EGF (EGF-IRDye). *In vitro* studies indicated that the U251-GFP cell line had 20-fold higher EGF uptake as compared to the 9L-GFP cell line, thus detection of the U251-GFP tumors over non-tumor-bearing control animals was expected to be better than detection of the 9L-GFP tumors. The relative average fluorescence difference between the average non-tumor-bearing control animals ($n=8$) and the tumor-bearing groups was calculated 24 h after IV administration of EGF-IRDye. The tumor-bearing groups had higher relative mean difference in the EGF-IRDye fluorescence as compared to control animals (mean relative difference: control=0.0057, 9L-GFP=0.23, U251-GFP=0.58) [Fig. 5(b)]. The mean fluorescence of the U251-GFP tumor-bearing mice was significantly higher than the control (p -value=0.001) while no significant difference was detected between the 9L-GFP tumor-bearing mice and the control (p -value=0.107). ROC analysis revealed that the U251-GFP tumors could be detected with 100% sensitivity and specificity over non-tumor-bearing control animals (AUC=1.0) using EGF-IRDye fluorescence [Fig. 5(b)]. Due to the low uptake of EGF-IRDye

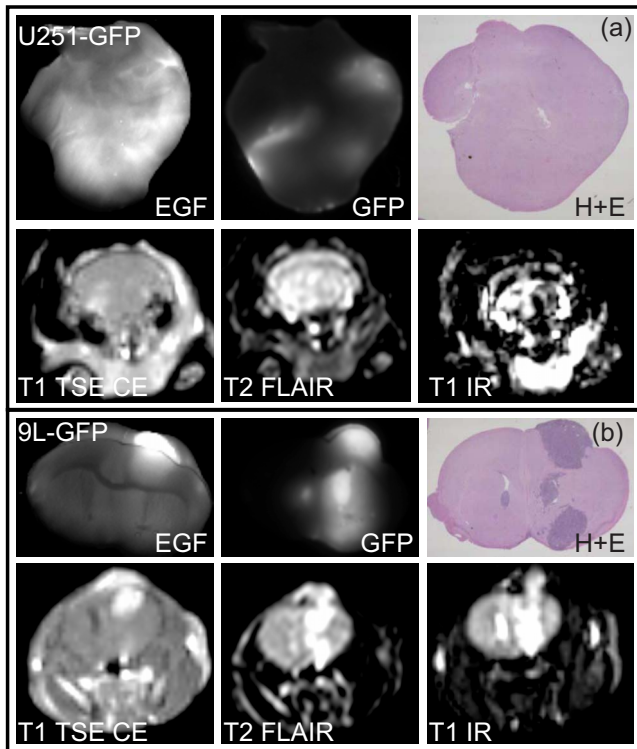


Fig. 6. Example EGF-IRDye detection of 9L-GFP and U251-GFP intracranial tumors. (a) *Ex vivo* EGF-IRDye, GFP, and H+E sections of a representative mouse from the U251-GFP group are shown in the first row. Qualitatively corresponding *in vivo* MRI images of the same section are shown in the second row. (b) *Ex vivo* EGF-IRDye, GFP, and H+E sections of a representative mouse from the 9L-GFP group are shown in the first row. Qualitatively corresponding *in vivo* MRI images of the same section are shown in the second row.

by the 9L-GFP tumors, ROC analysis of the detection of these tumors over non-tumor-bearing control animals revealed an AUC of 0.74.

A representative example of each tumor type was examined for EGF-IRDye uptake *ex vivo*. The U251-GFP tumors showed EGF-IRDye uptake corresponding to the size and shape of the tumor tissue, as seen when *ex vivo* GFP, EGF-IRDye, and HE images [Fig. 6(a)] were compared. In contrast, a representative 9L-GFP tumor-bearing mouse showed heterogeneous EGF-IRDye uptake which did not correspond to the tumor size and shape when the EGF-IRDye image was compared to corresponding GFP and HE images [Fig. 6(b)].

IV. DISCUSSION

Significant detection differences are seen between standard MR imaging sequences and functional optical spectroscopy for different glioma tumor models. Detection via tumor structure is difficult for diffusely growing tumor tissues, and diffuse optical measurement may significantly improve tumor detection when used to probe fluorescent proteins that are specific to the molecular features of a tumor. In contrast, optical imaging for well demarcated bulk tumors was less sensitive than MRI as standard MR sequences can generally provide 100% sensitivity and specificity in these cases. Glioma tumors are incurable and cause death from their dif-

fuse, infiltrative component, which is not easily visualized or resected and thus continues to grow following surgical intervention. Additionally in pediatric glioma some of the more problematic cases come in a diffuse morphology which is not as readily observed by standard contrast MR imaging.

Optical imaging of tumors is now widespread through most preclinical research centers, and optimization of the approach for detection of deep orthotopic tumors is an area which is developing,¹⁸ but is still limited in utility due to light sampling through bulk tissue. While many imaging systems operate in reflectance mode, where the source and detector are on the same side of the animal, detection of tumors deep in the tissue is generally not successful with this approach. Transmittance-style imaging of fluorescence is an effective way to improve signal, yet it requires careful system analysis, and is highly sensitive to the tissue geometry and signal normalization process.^{19–22} Commercial transmittance-style systems are now available, but measurements must be interpreted with care due to the nonlinear response and attenuation, as well as the effects of tissue curvature and tissue layers. However, since the light spreads throughout the tissue and is transmitted diffusely through the tissue, the ability of this scattered light field to sample tumors which are infiltrating and have a “diffuse growth morphology” would likely be good if utilized appropriately.²³

In the current study, a simulation of two different source-detector configurations, modeling the single channel, and multichannel transmission spectroscopy system was used to assess brain tumor detection at varied locations in the cranium. Brain tumor detection over non-tumor-bearing control animals was better for the two fiber optic source-detector configuration [Fig. 1(e)], then the eight fiber optic source-detector configuration [Fig. 1(f)] when the tumor was at the center of the brain. However, when the simulated tumor was more realistically placed in 1 mm in from the top left edge of the brain on all axes, tumor detection was better using the eight fiber optic source-detector configuration [Fig. 1(h)] than the two fiber optic source-detector configuration [Fig. 1(g)]. Thus, when the tumor was directly in the measurement plane, the two fiber optic configuration measured higher contrast difference than the eight fiber optic configuration. In the case of the eight fiber optic configuration, all measurements from around the head were averaged into a single number, and thus light path measurements that did not travel directly across the tumor tissue positioned at the center of the brain confounded the detection of the tumor by signal averaging.²³ Conversely, when the tumor was placed more realistically, the eight fiber optic configuration performed better than the two fiber optic configuration since the eight fiber optic configuration provided a more robust measurement of fluorescence signal from around the cranium as opposed to a single light path across the brain.

MRI is the gold standard for glioma tumor detection and is successful at brain tumor visualization. However, tumor detection and visualization are dependent on tumor growth pattern, where diffuse growth can be very difficult to detect by MR imaging. In the current study, glioma tumor detection

by MRI of the well-demarcated models or the diffusing growing tumor model was marginally dependent on the sequence and more dependent on the *in vivo* tumor growth pattern. The well-demarcated bulk tumors were readily detected by T1 TSE CE and T2 TSE MRI with 100% sensitivity and specificity [Figs. 4(a) and 4(b)]. These tumors appeared hyperintense by both T1 TSE CE and T2 TSE MRI and had sharp tumor borders that were easily visualized (Fig. 3). In contrast, the diffusely growing tumor model was difficult to detect via standard T1 TSE CE or T2 TSE imaging as well as T1 difference, T2 FLAIR, T1 IR, or T1 FFE sequences adapted for murine glioma imaging [Fig. 4(c)]. ROC analysis revealed a calculated AUC of 0.81 or less depending on the MRI sequence used. As illustrated by Fig. 2, MRI visibility was not necessarily based on the implanted brain tumor cell line, but rather the pattern of tumor growth. Three example mice with U251-GFP implanted tumors are shown where Fig. 2(a) shows a mouse with a well-demarcated tumor that was readily visible by T1 TSE CE MR, while Figs. 2(b) and 2(c) show diffusely growing tumor tissue that was difficult to discern via T1 TSE CE MR.

Two fluorescent probes were used evaluate brain tumor detection sensitivity using optical spectroscopy fluorescence to transmittance measurements. Intracellular, PpIX production was measured using the single channel spectroscopy system in all three murine glioma tumor models, albeit with differing levels of sensitivity and specificity. After the administration of the prodrug, ALA, exogenous, intracellular PpIX fluorescence was produced at different levels in each of the tumor bearing groups. Detection of tumor tissue by PpIX fluorescence was not dependent on growth pattern as seen by MRI, but rather was determined by tumor tissue metabolism. Intracellular PpIX production was increased in rapidly proliferating tumor tissue (Fig. 2) as compared to senescent cells at the center of a large bulk tumor (Fig. 3). Thus, tumor detection via PpIX fluorescence was improved for tumor tissue with high metabolic rate over tumor tissue that was senescent due to its large size and inability for further growth in the confined space of the cranium [Fig. 5(a)]. Due to the large size of the 9L-GFP tumors, detection was better by MRI than by functional metabolic fluorescence spectroscopy. The diffusely growing U251-GFP tumors were detected at a similar rate by either functional PpIX spectroscopy or MRI.

Alternative methods to use optical fluorescence of proteins are to label with a fluorescent tag and to choose proteins that are well tolerated by the biological system and very specific to the tumor being tested for. In this case, the extracellular signaling of this tumor line was probed by fluorescence using epidermal growth factor (EGF) conjugated to an infrared (IR) dye (EGF-IRDye). *In vitro* experiments show a 20-fold higher EGF uptake from the U251-GFP cell line as compared to the negative control 9L-GFP cell line. Mice bearing 9L-GFP and U251-GFP tumors were monitored using the fluorescence spectroscopy system after intravenous administration of the probe for up to 24 h. The relative difference from the average of the non-tumor-bearing control group ($n=8$) was calculated for each tumor type. The tumor-

bearing groups had higher relative average difference in mean EGF-IRDye fluorescence as compared to control animals (mean relative average difference: control=0.0057, 9L-GFP=0.23, U251-GFP=0.58) [Fig. 5(b)]. The mean fluorescence of the U251-GFP tumor-bearing mice was significantly higher than the control mice (p -value=0.001) while no significant difference was detected between the 9L-GFP tumor-bearing mice and the control group (p -value=0.107). ROC analysis revealed that the U251-GFP tumors could be detected with 100% sensitivity and specificity (AUC=1.0) [Fig. 5(b)]. As would be expected, the AUC for the EGF-negative 9L-GFP tumors was 0.74, better than *in vivo* PpIX detection, but significantly worse than tumor detection by MR.

Extracellular fluorescence measurement of EGF uptake showed higher signals in the diffusely growing tumor (U251-GFP) as compared to the well-demarcated tumor models. These diffusely growing tumors were able to be detected with 100% sensitivity and specificity via EGF-IRDye fluorescence spectroscopy [Fig. 5(b)], a vast improvement in detection over all MRI sequences, the best of which showed AUC=0.81. The detection of the well-demarcated tumors was better via EGF-IRDye fluorescence (AUC=0.74) than by PpIX fluorescence (AUC=0.59), however, nearly as not as reliable as detection via T1 TSE CE and T2 TSE MRI (AUC=1.0). The *in vivo* detection differences were confirmed through *ex vivo* EGF-IRDye uptake patterns which illustrated increased fluorescence intensity matching the size and shape of the tumor for the diffusely growing model [Fig. 6(a)] and heterogeneous uptake in the well-demarcated tumor model [Fig. 6(b)].

V. CONCLUSION

The studies completed here demonstrate a possible detection improvement over conventional MR imaging for diffuse glioma tumors through transmission spectroscopy of molecularly targeted fluorescent probes. The diffusely growing glioma model in this study was difficult to detect by MR imaging sequences including T1 TSE CE, T2 TSE, T2 FLAIR, T1 IR, T1 FFE, and T1 difference imaging where ROC analysis revealed at best an AUC=0.81. By comparison, when fluorescently labeled EGF was used for tumor detection ROC analysis revealed an AUC=1 and thus these tumors could be detected using transmission spectroscopy with 100% sensitivity and specificity, a vast improvement over detection via MRI. PpIX based transmission spectroscopy for diffuse glioma detection gave similar results to MRI and thus did not show significant tumor detection improvement, but may provide information about the metabolic status of the tumor tissue. Perhaps the most robust tumor information could be obtained through combined optical spectroscopy and MRI of a single tumor to assess both its structural and function status.

ACKNOWLEDGMENTS

This work has been supported by the National Cancer Institute through research Grant Nos. RO1CA109558 and

PO1CA084203. The authors would like to acknowledge Dr. Keith D. Paulsen for important advice and access to imaging facilities, as well as Dr. Hamid Dehghani and Dr. Scott C. Davis for light transport modeling assistance. The authors are grateful to LiCOR Biosciences for supply of some of the EGF-IRDye supply.

^{a)}Present address: Beth Israel Deaconess Medical Center, Harvard Medical School, Boston MA 02215; electronic mail: sgibbs@bidmc.harvard.edu

¹S. K. Ellika *et al.*, "Role of perfusion CT in glioma grading and comparison with conventional MR imaging features," *AJNR Am. J. Neuroradiol.* **28**, 1981–1987 (2007).

²A. Ree, R. Jain, J. Rock, M. Rosenblum, and S. C. Patel, "Direct infiltration of brainstem glioma along the cranial nerves," *J. Neuroimaging* **15**, 197–199 (2005).

³A. Laprie *et al.*, "Longitudinal multivoxel MR spectroscopy study of pediatric diffuse brainstem gliomas treated with radiotherapy," *Int. J. Radiat. Oncol., Biol., Phys.* **62**, 20–31 (2005).

⁴D. Hargrave, U. Bartels, and E. Bouffet, "Diffuse brainstem glioma in children: critical review of clinical trials," *Lancet Oncol.* **7**, 241–248 (2006).

⁵W. Stummer *et al.*, "Fluorescence-guided surgery with 5-aminolevulinic acid for resection of malignant glioma: a randomised controlled multicentre phase III trial," *Lancet Oncol.* **7**, 392–401 (2006).

⁶W. Stummer, H. J. Reulen, A. Novotny, H. Stepp, and J. C. Tonn, "Fluorescence-guided resections of malignant gliomas—an overview," *Acta Neurochir. Suppl. (Wien)* **88**, 9–12 (2003).

⁷D. Fukumura, L. Xu, Y. Chen, T. Gohongi, B. Seed, and R. K. Jain, "Hypoxia and acidosis independently up-regulate vascular endothelial growth factor transcription in brain tumors *in vivo*," *Cancer Res.* **61**, 6020–6024 (2001).

⁸L. Xu, D. Fukumura, and R. K. Jain, "Acidic extracellular pH induces vascular endothelial growth factor (VEGF) in human glioblastoma cells via ERK1/2 MAPK signaling pathway: mechanism of low pH-induced VEGF," *J. Biol. Chem.* **277**, 11368–11374 (2002).

⁹D. T. Delpy and M. Cope, "Quantification in tissue near-infrared spectroscopy," *Philos. Trans. R. Soc. Lond. B Biol. Sci.* **352**, 649–659 (1997).

¹⁰G. Alexandrakis, F. R. Rannou, and A. F. Chatziioannou, "Tomographic bioluminescence imaging by use of a combined optical-PET (OPET) system: a computer simulation feasibility study," *Phys. Med. Biol.* **50**, 4225–4241 (2005).

¹¹H. Dehghani *et al.*, "Near Infrared Optical Tomography using NIRFAST: Algorithms for Numerical Model and Image Reconstruction Algorithms," *Commun. Numer. Meth. Eng.* (in press).

¹²A. Moore, E. Marecos, M. Simonova, R. Weissleder, and A. Bogdanov, "Novel Gliosarcoma Cell Line Expressing Green Fluorescent Protein: A Model for Quantitative Assessment of Angiogenesis," *Microvasc. Res.* **56**, 145–153 (1998).

¹³S. C. Davis *et al.*, "Magnetic resonance-coupled fluorescence tomography scanner for molecular imaging of tissue," *Rev. Sci. Instrum.* **79**, 064302 (2008).

¹⁴B. W. Pogue and M. Patterson, "Review of tissue simulating phantoms for optical spectroscopy, imaging and dosimetry," *J. Biomed. Opt.* **13**(4), 11 (2006).

¹⁵J. L. Kovar, M. A. Johnson, W. M. Volcheck, J. Chen, and M. A. Simpson, "Hyaluronidase expression induces prostate tumor metastasis in an orthotopic mouse model," *Am. J. Pathol.* **169**, 1415–1426 (2006).

¹⁶V. Ntziachristos *et al.*, "Visualization of antitumor treatment by means of fluorescence molecular tomography with an annexin V-Cy5.5 conjugate," *Proc. Natl. Acad. Sci. U.S.A.* **101**, 12294–12299 (2004).

¹⁷X. Song, B. W. Pogue, D. Dehghani, S. Jiang, K. D. Paulsen, and T. D. Tosteson, "Receiver operating characteristic and location analysis of simulated near-infrared tomography images," *J. Biomed. Opt.* **12**, 054013 (2007).

¹⁸V. Ntziachristos, C. H. Tung, C. Bremer, and R. Weissleder, "Fluorescence molecular tomography resolves protease activity *in vivo*," *Nat. Med.* **8**, 757–760 (2002).

¹⁹V. Ntziachristos *et al.*, "Planar fluorescence imaging using normalized data," *J. Biomed. Opt.* **10**, 064007 (2005).

²⁰V. Ntziachristos, J. Ripoll, L. V. Wang, and R. Weissleder, "Looking and listening to light: the evolution of whole-body photonic imaging," *Nat. Biotechnol.* **23**, 313–320 (2005).

²¹V. Ntziachristos, C. Bremer, and R. Weissleder, "Fluorescence imaging with near-infrared light: new technological advances that enable *in vivo* molecular imaging," *Eur. Radiol.* **13**, 195–208 (2003).

²²V. Ntziachristos, C. Bremer, E. E. Graves, J. Ripoll, and R. Weissleder, "In vivo tomographic imaging of near-infrared fluorescent probes," *Mol. Imaging* **1**, 82–88 (2002).

²³S. Gibbs, B. Chen, J. O'Hara, P. Hoopes, T. Hasan, and B. Pogue, "Protoporphyrin IX level correlates with number of mitochondria, but increase in production correlates with tumor cell size," *Photochem. Photobiol.* **82**, 1334–1341 (2006).